

Geometric Methods for Spherical Data, with Applications to Cosmology

Javier Carrón Duque^{1,2} and Domenico Marinucci³

¹Department of Physics, University of Rome Tor Vergata, Roma, Italy, 00133; email: javier.carron@roma2.infn.it

²Sezione INFN Roma 2, Roma, Italy, 00133

³Department of Mathematics, University of Rome Tor Vergata, Roma, Italy, 00133; email: marinucc@mat.uniroma2.it

Xxxx. Xxx. Xxx. Xxx. YYYY. AA:1–25

This article's doi:
10.1146/((please add article doi))

Copyright © YYYY by Annual Reviews.
All rights reserved

Keywords

cosmic microwave background, spherical random fields, spherical harmonics, needlets, stochastic geometry, polarization

Abstract

This survey is devoted to recent developments in the statistical analysis of spherical data, with a view to applications in Cosmology. We will start from a brief discussion of Cosmological questions and motivations, arguing that most Cosmological observables are spherical random fields. Then, we will introduce some mathematical background on spherical random fields, including spectral representations and the construction of needlet and wavelet frames. We will then focus on some specific issues, including tools and algorithms for map reconstruction (*i.e.*, separating the different physical components which contribute to the observed field), geometric tools for testing the assumptions of Gaussianity and isotropy, and multiple testing methods to detect contamination in the field due to point sources. Although these tools are introduced in the Cosmological context, they can be applied to other situations dealing with spherical data. Finally, we will discuss more recent and challenging issues such as the analysis of polarization data, which can be viewed as realizations of random fields taking values in spin fiber bundles.

Contents

1. BACKGROUND: COSMOLOGICAL MOTIVATIONS	2
2. MATHEMATICAL FOUNDATIONS	4
2.1. Spectral Representation for Isotropic Spherical Random Fields	4
2.2. On the Meaning of Asymptotics in Cosmology	5
3. CMB MAP RECONSTRUCTION AND COMPONENT SEPARATION	8
4. POINT SOURCE DETECTION AND SEARCH FOR GALAXY CLUSTERS	9
5. TESTING FOR GAUSSIANITY AND ISOTROPY	12
6. DIRECTIONS FOR FURTHER RESEARCH	15
A. SPHERICAL HARMONICS AND THEIR MAIN PROPERTIES	22
B. THE SPECTRAL REPRESENTATION THEOREM	24

1. BACKGROUND: COSMOLOGICAL MOTIVATIONS

The status of Cosmology as an observational Science has experienced a dramatic shift in the last two decades. Until about the year 2000, Cosmology was known as a data-starved science: important experiments had been carried over in a number of fields, but the amount and quality of data were very far from the level needed to produce precise estimates of parameters and conclusive tests of most Cosmological Models; the situation has changed completely in the last couple of decades, when a number of experiments have improved the size and precision of existing observations by several orders of magnitude.

To name only a few such experiments, the Cosmic Microwave Background (CMB; to be discussed at length below) has been probed by the satellite experiments WMAP and Planck, by several balloon-borne and by ground-based observatories, and it is going to be further investigated by the forthcoming satellite mission LiteBIRD; Gamma rays sources have been probed by Satellite Missions Fermi-LAT and AGILE, and from several observatories on the ground; ultra-high energy cosmic rays are investigated by huge international collaborations such as the Pierre Auger observatory; Cosmic Neutrinos are the object of investigation by IceCube; Gravitational Waves have been detected by the LIGO–Virgo Collaboration and will be further probed in the next decades by a new generation of observatories; radio sources are probed by huge collaborations such as SKA, whereas the Large Scale Structure of the Universe and weak gravitational lensing are the object of upcoming missions such as Euclid.

A remarkable feature of all the datasets produced by these observations is the following: they are all defined on the sphere S^2 . For reasons of space and clarity, we will concentrate most of the discussion below on the CMB, but the tools that we shall introduce for spherical data analysis are relevant for many of the other applications as well.

To understand the CMB radiation, let us recall the Standard Cosmological Model: it states that the Universe (or the Universe that we currently observe) started 13.7 Billion years ago in a very hot and dense state, filled by a plasma of electrons, photons and protons (we note that this is a large oversimplification, but it does fit our purposes, see, *e.g.*, Dodelson (2003), Durrer (2008), Vittorio (2018), for a more detailed description). Matter was completely ionized, meaning that the mean kinetic energy of the electrons was higher than the electromagnetic potential of the protons, and no stable atoms formed: free electrons have a much larger "scattering surface", *i.e.*, probability to interact with a photon, so that

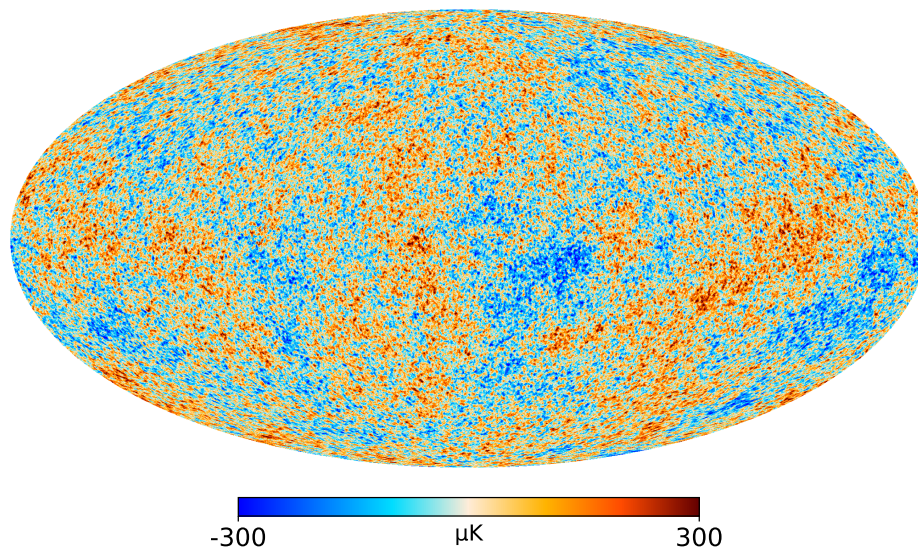


Figure 1

CMB Temperature field as measured by the Planck satellite. This is a snapshot of the Early Universe, allowing us to study the components and evolution of the Universe. This spherical field is projected here with a Mollweide projection in galactic coordinates.

the mean free path of the latter was very short and the Universe was basically opaque to light. As the Universe expanded, the energy density and the kinetic energy of the electrons decreased to a point where it was no longer enough to resist the attraction of the protons: at this stage, stable hydrogen atoms formed, and the Universe became transparent to light. In this so-called “Age of Recombination”, which is now estimated to have taken place about 377,000 years after the Big Bang, the Universe became transparent to light and these primordial photons started to move freely across the Universe. Hence, one of the key predictions of the model is that we should live embedded into this relic radiation, providing an image of the Universe as it was 13.7 billion years ago. These photons, now observed in microwave frequencies and in every direction on the sky, constitute the Cosmic Microwave Background.

Although the first papers predicting the CMB radiation date back to around 1945, the first observational proof of its existence was given in a celebrated experiment by Penzias and Wilson in 1965. However, it was only in the current century that sophisticated satellite missions such as WMAP and, especially, Planck managed to produce high-resolution low-noise full-sky maps of the *Last Scattering Surface*, see **Figure 1**, Planck Collaboration (2020a), and Bobin et al (2014). In the next Section, we shall introduce the mathematical formalism that we will require for the statistical analysis of these maps.

2. MATHEMATICAL FOUNDATIONS

2.1. Spectral Representation for Isotropic Spherical Random Fields

Formally, a spherical random field is a collection of real random variables indexed by points on the sphere, *i.e.*, $\{T : \Omega \times \mathbb{S}^2 \rightarrow \mathbb{R}\}$, for some suitable underlying probability space $\{\Omega, \mathfrak{S}, \mathbb{P}\}$; without loss of generality we take these random variables to be zero mean $\mathbb{E}[T(x)] = 0$, we assume they have finite variance $\mathbb{E}[T^2(x)] < \infty$, and we assume isotropy, meaning that the field is invariant in law to rotations:

$$T(x) \stackrel{Law}{=} T(gx) \text{ for all } g \in SO(3).$$

Isotropy can be viewed as broadly analogous to the (strong) stationarity that allows to develop the classical spectral representation approach when dealing with Time Series, see *e.g.* Brockwell & Davis (2006). Indeed, under these conditions, a Spectral Representation Theorem holds on the sphere; more precisely, we have (see the Appendix or Marinucci & Peccati 2011)

$$T(x, \omega) = \sum_{\ell=0}^{\infty} \sum_{m=-\ell}^{\ell} a_{\ell m}(\omega) Y_{\ell m}(x), \quad (1)$$

where the identity holds both in $L^2(\Omega)$ and in $L^2(\Omega \times \mathbb{S}^2)$; here we have written explicitly the random variables as functions of $\omega \in \Omega$ to highlight the decoupling between random components depending on Ω and deterministic components depending on \mathbb{S}^2 .

The deterministic functions $\{Y_{\ell m}\}$ are the *spherical harmonics* and, for fixed ℓ , they form an orthonormal basis of the eigenspace of the Spherical Laplacian operator $\Delta_{\mathbb{S}^2}$, with eigenvalues corresponding to $-\lambda_{\ell} = -\ell(\ell + 1)$. They indeed satisfy

$$\Delta_{\mathbb{S}^2} Y_{\ell m} = -\lambda_{\ell} Y_{\ell m}, \quad \ell = 0, 1, 2, \dots, \quad m = -\ell, \dots, \ell; \quad (2)$$

again, more details and definitions are given in the Appendix. We therefore have a decomposition into a set of eigenfunctions, along different frequencies basically corresponding to the square root of the corresponding eigenvalues (known as *multipoles* ℓ in the spherical case). The most important message to remember, also for its statistical consequences, is that in the case of the sphere there are $2\ell + 1$ independent components corresponding to each “frequency” (multipole) ℓ : this fact will play a crucial role in the asymptotic results to follow.

By expressing the field $T(x)$ in the spherical harmonics base according to Equation 1, we obtain the *random spherical harmonics coefficients* $\{a_{\ell m}\}$. They form an array of zero-mean, complex valued random variables with covariance given by

$$\mathbb{E}[a_{\ell m} \overline{a_{\ell' m'}}] = \delta_{\ell}^{\ell'} \delta_m^{m'} C_{\ell};$$

in other words, they are uncorrelated whenever ℓ or m differ from ℓ', m' and they have variance given by the non-negative sequence $\{C_{\ell}\}$, called the *angular power spectrum* of the random field $T(x)$. The covariance function of the field can be expressed as (Schoenberg’s Theorem):

$$Cov(T(x_1), T(x_2)) = \mathbb{E}[T(x_1), T(x_2)] = \sum_{\ell=0}^{\infty} \frac{2\ell + 1}{4\pi} C_{\ell} P_{\ell}(\langle x_1, x_2 \rangle),$$

where $P_\ell(\cdot)$ is the sequence of Legendre polynomials, to be introduced in the Appendix and $\langle x, y \rangle$ is the standard scalar product.

It should also be noted that the spherical harmonic coefficients can in principle be recovered from the observations of the field (up to some statistical difficulties that we shall discuss below) by means of the inverse spherical harmonic transform:

$$a_{\ell m} = \int_{\mathbb{S}^2} T(x) \overline{Y_{\ell m}(x)} dx . \quad (3)$$

From a cosmological perspective, the angular power spectrum of the CMB, C_ℓ , is a main source of information. It is sensitive to the exact values of the cosmological parameters, such as the amount of baryonic matter, Dark Matter, or Dark Energy in the Universe (Planck Collaboration 2020c,d). Modern CMB observations such as Planck are able to measure the angular power spectrum with unprecedented precision, leading to subpercentage uncertainties in most cosmological parameters; because of this, it is commonly said that the field is now in an era of *precision Cosmology*.

2.2. On the Meaning of Asymptotics in Cosmology

A deep foundational question must be addressed when dealing with cosmological data. By definition, Cosmology is a science based on a single observation—our Universe; then, how is it possible to apply asymptotic statistics tools?

The asymptotic theory which is used in this framework is meant in the high-frequency sense, rather than the large domain one; it is strictly related to so-called fixed-domain asymptotics, the common framework under which geophysical data are usually handled (see, *e.g.*, Loh 2005, 2015, and the references therein). It is assumed that inverse Fourier transforms like Equation 3 are evaluated for $\ell = 1, 2, \dots, L_{\max}$, where L_{\max} grows from one experiment to the other. This setting fits exactly the reality of data collection in Cosmology: a pioneering experiment like COBE had a resolution to reach an L_{\max} of the order of 20–30, a number which was raised to 600–800 for WMAP and subsequently to about 2000 by Planck; in the next generation of experiments, these values could grow further by a factor of at least 2 or 3. More precisely, observations are collected on a grid of sampling points that depend on the resolution of the experiment: it arrives to a cardinality of about 12×1024^2 points for Planck. By means of these observations, integrals as Equation 3 are approximated as Riemann sums; the order of the multipoles for which this approximation can work depends on the resolution of the grid.

In practice, however, the observations are not available with the same level of accuracy on the full sphere: there are some regions of the sky where foreground contaminants such as the Milky Way cannot be removed efficiently. It is then convenient to introduce some form of spherical wavelet transform, as we shall do in the remainder of this section.

In particular, we will consider needlets: a form of spherical wavelets which was introduced by Narcowich et al (2006a,b) in the mathematical literature (see also Geller & Mayeli 2009a,b,c) and then to the Cosmological and Statistical communities by Baldi et al (2009a,b), Marinucci et al (2008), see also Scodeller et al (2011) and the references therein. The basic idea behind needlets can be summarized as follows. Consider first the operator

which goes from the random field $T(x)$ to its Fourier components $T_\ell(x)$:

$$\begin{aligned} T_\ell(x) &= \sum_{m=-\ell}^{\ell} a_{\ell m} Y_{\ell m}(x) = \sum_{m=-\ell}^{\ell} \int_{\mathbb{S}^2} T(z) \bar{Y}_{\ell m}(z) dz Y_{\ell m}(x) \\ &= \int_{\mathbb{S}^2} T(z) \sum_{m=-\ell}^{\ell} \bar{Y}_{\ell m}(z) Y_{\ell m}(x) dz = \int_{\mathbb{S}^2} T(z) \frac{2\ell+1}{4\pi} P_\ell(\langle z, x \rangle) dz , \end{aligned}$$

where the last equality comes from Equation 8 in the Appendix. In other words, the Fourier components can be realized as the projections of the fields on the “frequency” (multipole) component ℓ by means of the kernel operator $\frac{2\ell+1}{4\pi} P_\ell(\langle x, \cdot \rangle)$. These multipole components of the field T_ℓ are perfectly localized in harmonic domain (as they are projected onto a single multipole) at the expense of losing all spatial localization. This can be a problem when different parts of the sphere are observed with different levels of noise or with incomplete observations.

The idea of needlets is to partially give up the perfect localization in the harmonic domain in order to obtain better localization properties in the real domain. In particular, let us now consider a smooth (possibly C^∞) non-negative function $b(\cdot)$, supported in the compact domain $(\frac{1}{B}, B)$, with $B > 1$; we additionally impose that its square satisfies the partition of unity property, namely

$$\sum_{j=0}^{\infty} b^2\left(\frac{\ell}{B^j}\right) \equiv 1 , \text{ for all } \ell = 1, 2, \dots$$

Note that the elements in the sum are different from zero only for $\ell \in (B^{j-1}, B^{j+1})$. Now consider also a grid of cubature points $\{\xi_{jk} \in \mathbb{S}^2\}_{j=1,2,\dots;k=1,2,\dots,N_j}$, with growing cardinality N_j of order B^{2j} , nearly equispaced so that $d_{\mathbb{S}^2}(\xi_{jk}, \xi_{j'k'}) \simeq cB^{-j}$, where we have introduced the spherical geodesic distance

$$d_{\mathbb{S}^2}(x, y) := \arccos(\langle x, y \rangle) .$$

The needlet projection coefficients are defined by

$$\beta_{jk} := \int_{\mathbb{S}^2} T(x) \psi_{jk}(x) dx , \quad \psi_{jk}(x) := \sum_{\ell} b\left(\frac{\ell}{B^j}\right) \frac{2\ell+1}{4\pi} P_\ell(\langle x, \xi_{jk} \rangle) \sqrt{\lambda_{jk}} ,$$

where $\{\lambda_{jk}\}$ are cubature weights, which can be chosen in such a way as to ensure the identity

$$\sum_{k=1}^{N_j} Y_{\ell m}(\xi_{jk}) \overline{Y_{\ell' m'}(\xi_{jk})} \lambda_{jk} = \delta_\ell^{\ell'} \delta_m^{m'} , \text{ for all } \ell, \ell' \leq [B^{j+1}] .$$

It is then easy to see that the following reconstruction formula holds:

$$T(x) = \sum_{jk} \beta_{jk} \psi_{jk}(x) = \sum_j \tilde{T}_j(x) ,$$

where the needlet components are defined by

$$\tilde{T}_j(x) = \sum_{\ell=0}^{\infty} b^2\left(\frac{\ell}{B^j}\right) T_\ell(x) . \quad (4)$$

Alternatively, we could introduce the *needlet projection kernel*

$$\Psi_j(x, y) = \sum_{\ell=0}^{\infty} b^2 \left(\frac{\ell}{B^j} \right) \frac{2\ell+1}{4\pi} P_\ell(\langle x, y \rangle)$$

which acts on the field $T(\cdot)$ in such a way that

$$\begin{aligned} \Psi_j : T(x) &\rightarrow \int_{\mathbb{S}^2} T(z) \Psi_j(z, x) dz = \\ &= \sum_{\ell=0}^{\infty} b^2 \left(\frac{\ell}{B^j} \right) \int_{\mathbb{S}^2} T(z) \frac{2\ell+1}{4\pi} P_\ell(\langle z, x \rangle) dz = \tilde{T}_j(x) . \end{aligned}$$

Therefore, it is now readily seen that this needlet projection operator projects the field $T(\cdot)$ on a linear combination of eigenfunctions T_ℓ , for $\ell \in (B^{j-1}, B^{j+1})$. More importantly, the needlet kernel projector enjoys much better localization properties than the simple Legendre projector; indeed, it has been shown (see Narcowich et al 2006a,b, Geller & Mayeli 2009a) that for all $M \in \mathbb{N}$ there exists a positive constant C_M s.t.

$$|\Psi_j(x, y)| \leq C_M \frac{B^{2j}}{(1 + B^j d_{\mathbb{S}^2}(x, y))^M} . \quad (5)$$

In words, this means that for any fixed angular distance, the kernel decays to zero faster than any polynomial in j . As a consequence, it is possible to evaluate needlet projections even in the case of sky maps which are only partially observed, given that, for any “masked” (*i.e.*, unobservable) region $G \subset \mathbb{S}^2$ and $x \in \mathbb{S}^2 \setminus G$ we have

$$\begin{aligned} \int_{\mathbb{S}^2 \setminus G} T(z) \Psi_j(z, x) dz &= \int_{\mathbb{S}^2} T(z) \Psi_j(z, x) dz - \int_G T(z) \Psi_j(z, x) dz \\ &= \tilde{T}_j(x) + R_j(x) , \end{aligned}$$

where

$$\begin{aligned} \mathbb{E}[|R_j(x)|] &\leq \int_G \mathbb{E}[|T(z)|] |\Psi_j(z, x)| dz \\ &\leq Const \times \int_G |\Psi_j(z, x)| dz \\ &\leq Const \times C_M \int_G \frac{B^{2j}}{(1 + B^j d_{\mathbb{S}^2}(x, z))^M} dz \\ &\leq C'_M \times 4\pi \times B^{j(2-M)} \times d_{\mathbb{S}^2}^{-M}(x, G) \rightarrow 0 , \text{ as } j \rightarrow \infty , \end{aligned}$$

where $d_{\mathbb{S}^2}(x, G)$ is defined as the infimum of the distances between x and the points of G . The decay to zero is itself super-exponential, and a very broad numerical and empirical evidence has shown that needlet components of spherical random fields are minimally affected by unobserved regions, in the high-frequency sense, and for reasonable amounts of masked information.

Needlet fields enjoy another very important property for statistical analysis. In particular, it has been established that (see Baldi et al 2009b)

$$\left| \text{Corr}(\tilde{T}_j(x), \tilde{T}_j(y)) \right| \leq Const \times \frac{1}{(1 + B^j d_{\mathbb{S}^2}(x, y))^M} ;$$

in other words, the correlation between the needlet fields evaluated on any two points decays faster than any polynomial. At first sight, one may think this is a direct consequence of the localization properties of the needlet kernel projector (see Equation 5), but this is not the case: uncorrelation is not in general a consequence of kernel localization. To understand this point, consider the extreme case of a delta-like projector such that $\delta_x : T \rightarrow T(x)$; this is obviously an example of perfect localization in real space, but nevertheless the correlation between any two projected components $T(x)$ and $T(y)$ does not decay to zero in any meaningful sense. It is the combination of localization in real and harmonic space, a defining feature of needlets, that makes fast uncorrelation possible.

In the next Section, we show how these uncorrelation properties make it possible to study principled statistical inference with an asymptotic justification.

3. CMB MAP RECONSTRUCTION AND COMPONENT SEPARATION

The first statistical issue we shall consider is the so-called CMB map reconstruction (sometimes also called component separation or foreground removal). This is the cosmological instance of the image reconstruction issues that are common in many fields, and because of this, the techniques introduced in this chapter are likely to be applicable to many different areas.

The problem arises from a very natural question: when observing the celestial sky, how can you distinguish CMB radiation from the many other galactic and extragalactic sources that lie between us and the last scattering surface? The key remark is that CMB observations are collected on many different electromagnetic frequencies, where they follow a Planckian black-body emission governed by a single (temperature) parameter (see Durrer 2008, Planck Collaboration 2020b, Axelsson et al 2015). Therefore, we can decompose the observation at frequency ν_k and point x , $T(x, \nu_k)$, after suitable transformations, in the following way:

$$T(x; \nu_k) = T(x) + F(x; \nu_k) + N(x, \nu_k) ,$$

where $N(x, \nu_k)$ denotes instrumental noise and $F(x; \nu_k)$ are “foreground residuals”, *i.e.* the collection of emission by galactic dust, astrophysical sources, and other mechanisms both from within the Galaxy and from outside it. The crucial identifying assumption is that the CMB “signal” $T(x)$ is constant across the different electromagnetic channels (although by no means constant over the sky directions $x \in \mathbb{S}^2$). Assume as a starting point that the noise $N(\cdot)$ has zero mean, constant variance and is uncorrelated over different electromagnetic frequencies; for the foreground, assume again that it has finite variance, and that its variance covariance matrix over different channels is given by

$$\mathbb{E} \left[F(x; \cdot) F(x; \cdot)^T \right] = \Omega .$$

The best linear unbiased estimates of $T(x)$, viewed as a fixed parameter at a given x , is then simply given by the generalized least squares solution.

$$\widehat{T}_{ILC}(x) = \left\{ P^T (\Omega + \sigma_N^2 I_K)^{-1} P \right\}^{-1} P^T (\Omega + \sigma_N^2 I_K)^{-1} T(x, \cdot) ,$$

where $P = (1, 1, \dots, 1)^T$ is the K -dimensional vector of ones, and by $T(x, \cdot)$ we mean the K -dimensional column vector with the observations across the different frequencies. This map-making algorithm is known as ILC (Internal Linear Combination) in the cosmological

literature. To be implemented, it requires an estimate of the covariance matrix Ω ; here is where the needlet approach can come into play.

The covariance matrix Ω represents the dependence structure and the overall magnitude of different foregrounds over different frequencies. This covariance varies wildly over different regions and over different scales: some foregrounds are dominant over large scales (*e.g.*, galactic dust) whereas other dominates on smaller scales (localized sources). To take into account the fact that variance can be different across different scales, the idea is to introduce the *NILC* (Needlet Internal Linear Combination) map-making algorithms, defined by (see Remazeilles et al 2011, and references therein)

$$\hat{T}_{NILC;j}(x) = \left\{ P^T \left(\hat{\Omega}_j + \sigma_N^2 I_K \right)^{-1} P \right\}^{-1} P^T \left(\hat{\Omega}_j + \sigma_N^2 I_K \right)^{-1} \tilde{T}_j(x, \cdot),$$

$$\hat{T}_{NILC}(x) = \sum_j \hat{T}_{NILC;j}(x),$$

where the covariance matrix Ω_j is estimated in a first step as

$$\hat{\Omega}_j = \frac{1}{4\pi} \int_{\mathbb{S}^2} (T(x; \nu_k) - \bar{T}(x)) (T(x; \nu_k) - \bar{T}(x))^T dx, \quad \bar{T}(x) = \frac{1}{K} \sum_k T(x; \nu_k).$$

As a second step (see, *e.g.*, Carones et al (2022c) and the references therein), one may take into account the spatial variability of the matrices $\Omega = \Omega(x)$, another task that can be addressed by needlets because of their spatial localization. The idea is then to partition the celestial sky into subregions A_r , with $r = 1, \dots, R$, such that $A_{r_1} \cap A_{r_2} = \emptyset$ and $\cup_{r=1}^R A_r = \mathbb{S}^2$. We can write now

$$\hat{\Omega}_{j,r} = \frac{1}{4\pi} \int_{A_r} (T(x; \nu_k) - \bar{T}(x)) (T(x; \nu_k) - \bar{T}(x))^T dx$$

$$\hat{T}_{NILC;j,r}(x) = \left\{ P^T \left(\hat{\Omega}_{j,r} + \sigma_N^2 I_K \right)^{-1} P \right\}^{-1} P^T \left(\hat{\Omega}_{j,r} + \sigma_N^2 I_K \right)^{-1} \tilde{T}_j(x, \cdot), \quad x \in A_r,$$

$$\hat{T}_{NILC;r}(x) = \sum_j \hat{T}_{NILC;j,r}(x), \quad x \in A_r.$$

This method has proven to be very efficient and compares favorably with other existing techniques, see again Carones et al (2022c) for further discussion.

For the rest of this paper, we shall assume to be dealing with maps that have been made according to one of these procedures: in the next two sections, we discuss how to test for residuals point sources and for deviations from the assumptions of isotropy and Gaussianity.

4. POINT SOURCE DETECTION AND SEARCH FOR GALAXY CLUSTERS

After a CMB map has been built from observations, as discussed in the previous Section, a natural question to ask is whether all the foreground contaminants have been properly removed. In this Section, we focus on so-called point sources: these are mainly galaxies or clusters of galaxies which appear as point-like local maxima in the maps (Planck Collaboration 2015).

The proper approach to handling such issues is clearly a form of multiple testing. Indeed, for an experiment like Planck, there are several thousand local maxima that could be

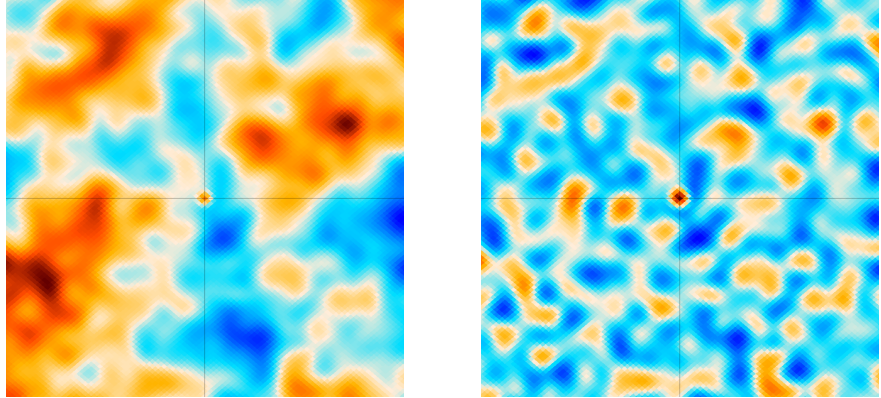


Figure 2

Effect of a point source on the CMB. On the left, CMB Temperature $T(x)$; on the right, a single needlet component, \tilde{T}_j . A point source has been introduced in the center of the map. The signal-to-noise ratio at the peak in this example goes from 0.4 to 4.4. Both images are $3^\circ \times 3^\circ$ patches of the sky.

identified as potential candidates for point sources: at each of these locations one may wish to run a significance test, but controlling the size of the test is then a daunting task. Very recently, this topic has been addressed in Carrón Duque et al (2019), Cheng et al (2020) by means of a variation in the so-called STEM (Smoothing and Testing Multiple Hypotheses) algorithm, see also Schwartzman et al (2011), Cheng & Schwartzman (2015, 2017, 2018), Cammarota et al (2016).

The idea of the procedure is rather natural and can be explained as follows. Because we are looking for point sources, large-scale fluctuations can be considered to produce just noise without information on the signal; in the first step, it is then natural to filter the map with a needlet transform and consider only the needlet components \tilde{T}_j (as defined in Equation 4), for “high enough” j , as we will discuss later. This procedure does increase the signal-to-noise ratio considerably, as illustrated in **Figure 2**, see also Scodeller et al (2012), Scodeller & Hansen (2012).

In a second step, we focus on the candidate sources, which correspond to the local maxima of the field \tilde{T}_j . Our aim is to establish the p -value of each of these local maxima. Therefore, we need to study the density of these maxima. It turns out that an exact result can be given (see Cheng et al 2020); we shall denote the probability density of maxima by f_j .

The expected density of maxima f_j is compared to the observed distribution in a single realization in **Figure 3**, for a needlet-filtered map at $B = 1.2$, $j = 39$. At these small scales, corresponding to the size of point sources, the theoretical expectation is remarkably close to the realized distribution, even when considering a single map.

We are then in the position to compute the p -value of each maximum: it is the probability of the maximum being larger than $\tilde{T}_j(\xi_k)$, with $k = 1, 2, \dots, K$ for the K maxima located

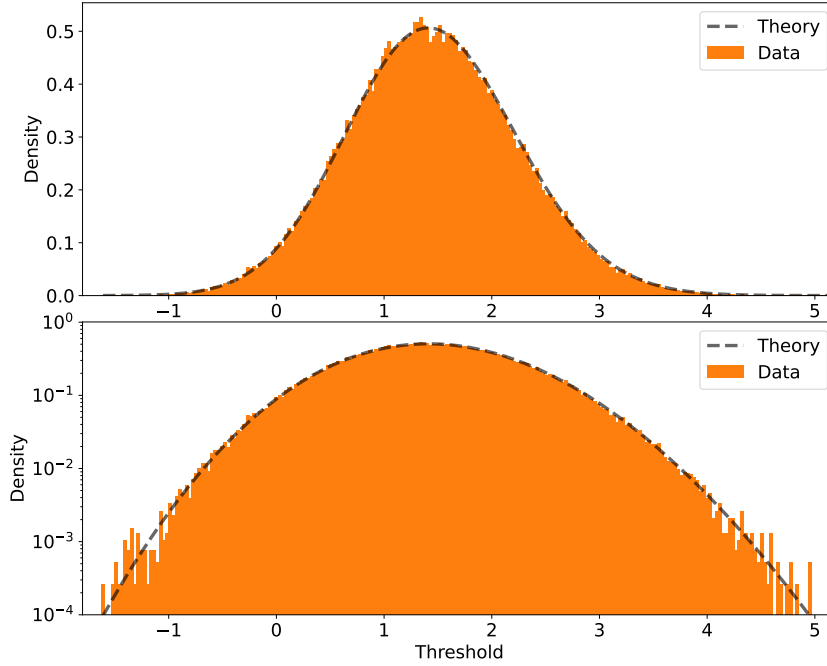


Figure 3

Distribution of the maxima of a needlet-filtered map, \tilde{T}_j with a small-scale needlet ($B = 1.2$, $j = 35$). In dashed black line, the theoretical prediction, f_j ; in orange bars, the realization on a single map. Top: linear scale. Bottom: logarithmic scale. It can be seen that the maxima density closely follows the prediction, even in a single realization.

at $\xi_1, \dots, \xi_K \in \mathbb{S}^2$. Therefore, the p -value of each maximum is

$$p_{k,j} := \int_{\tilde{T}_j(\xi_k)}^{\infty} f_j(u) du .$$

As a third step, we implement a Benjamini-Hochberg procedure for the identification of point sources (Benjamini & Hochberg 1995). To this aim, let us first reorder the p -values and sources so that they are increasing, $p_{(1),j} \leq p_{(2),j} \leq \dots \leq p_{(K),j}$; we then fix a value $0 < \alpha < 1$, corresponding to the expected proportion of False Discoveries that we are willing to tolerate among the reported Point Sources. Namely, we consider ξ_k to be the location of a Point Source whenever

$$u_{k,j} := p_{(k),j} - \alpha \frac{k}{K} < 0 ,$$

that is, when the $(k)^{\text{th}}$ ordered p -value is smaller than α times the expected p -value of the $(k)^{\text{th}}$ maximum under the null hypothesis of a purely Gaussian field.

The technical analysis of the properties of this procedure is based on a result of some independent interest, namely the high-frequency ergodicity of the empirical distribution of the maxima. In other words, it turns out to be possible to show that, as $j \rightarrow \infty$, for all fixed $u \in \mathbb{R}$

$$\frac{\text{Card}\left\{\tilde{T}_j(\xi_k) : \tilde{T}_j(\xi_k) > u\right\}}{\int_u f_j(x)dx} \xrightarrow{p} 1.$$

In turn, this result follows from the Kac–Rice representation of maxima and a high-frequency uncorrelation result on the gradient and Hessian of the needlet fields, see Cheng et al (2020) for more discussion and details.

The previous result forms the mathematical basis for establishing the two main properties of the Benjamini-Hochberg procedure in this context, namely

(a) False Discovery Rate control: as $j \rightarrow \infty$, we have that

$$\mathbb{E}\left[\frac{\text{Card}\left\{\tilde{T}_j(\xi_k) : u_{k,j} < 0 \text{ and no point source at } \xi_k\right\}}{\text{Card}\left\{\tilde{T}_j(\xi_k) : u_{k,j} < 0\right\}}\right] < \alpha$$

(b) Power control: as $j \rightarrow \infty$, the proportion of point sources that are detected converges to unity.

Actually, the result established in Cheng et al (2020) is stronger than (b), because the number of sources is allowed to grow with j , in an effort to mimic in this context a high-dimensional framework where the complexity of the signal (point sources) grows with the amount of observations. The approach described here was successfully applied to Planck CMB temperature maps and led to the possible discovery of a previously undetected source, see Carrón Duque et al (2019) for more details.

A final remark on this topic: in this section, the procedure we have introduced is based on the framework where the signal is made up by the sources to be detected, whereas noise is the given by a random Gaussian field, namely the CMB radiation which we consider as signal for most of the paper. This is sometimes summarized by the ironical motto “*your noise is my signal*” in some papers in this area. In the next section, we will further probe goodness-of-fit tests for the basic assumptions on the random fields at hand, namely Gaussianity and isotropy.

5. TESTING FOR GAUSSIANTY AND ISOTROPY

A crucial assumption to be investigated on spherical random fields is whether they are actually Gaussian and isotropic. A very important tool for this task is the so-called *Lipschitz–Killing Curvatures*; in the cosmological literature, the term “Minkowski functionals” is more often used, but the two definitions are equivalent up to some scaling constants and reordering of indexes.

The proper definition of Lipschitz-Killing Curvatures requires some geometric background. Let us first consider some convex set $A \subset \mathbb{R}^d$, and let us define the *Tube* of radius r around A as the set of points at distance smaller or equal than r from A :

$$\text{Tube}(A, r) := \left\{x \in \mathbb{R}^d : d(x, A) \leq r\right\}.$$

The *Tube Formula* (see Adler & Taylor 2007, 2011) proves that the volume of the Tube admits a finite-order Taylor expansion into powers of r :

$$\text{Meas} \{ \text{Tube}(A, r) \} = \sum_{i=0}^d \omega_{d-i} \mathcal{L}_i(A) r^i, \text{ where } \omega_i = \frac{\pi^{i/2}}{\Gamma(\frac{i}{2} + 1)},$$

$\Gamma(\alpha) = \int_0^\infty t^{\alpha-1} \exp(-t) dt$ denoting the Gamma function and ω_i represents the volume of the i -dimensional unit ball ($\omega_0 = 1, \omega_1 = 2, \omega_2 = \pi, \omega_3 = \frac{4}{3}\pi, \dots$). The coefficients $\mathcal{L}_i(A)$ are the so-called Lipschitz-Killing Curvatures of A ; for instance, in two-dimensional space there are three of them, equal to the area, half the boundary length, and the Euler–Poincaré Characteristic of the set A . The latter is a topological invariant that plays a crucial role in Mathematics: in the two-dimensional case, it is equivalent to the number of connected components of A minus its “holes”. It can be shown that any sufficiently regular functional of A can be written in terms of the Lipschitz-Killing Curvatures alone; in this sense, they can be viewed as some sort of sufficient statistic for the information encoded into A , see again Adler & Taylor (2007, 2011).

The Lipschitz-Killing Curvatures (or equivalently the Minkowski Functionals, which are the same quantities up to some constants and relabelling of indexes) are one of the most popular statistical tools for Cosmological data analysis. One reason for their popularity is that, quite surprisingly, it is possible to give simple analytic forms for their expected values, under the null assumptions of Gaussianity and isotropy: they are hence very natural tools for goodness-of-fit tests. More precisely, let us define the derivative of the covariance function at the origin as

$$\mu^2 := \left. \frac{\partial}{\partial y} \Gamma(\langle x, y \rangle) \right|_{y=x} = \sum_{\ell} \frac{2\ell + 1}{4\pi} \frac{\lambda_{\ell}}{2} C_{\ell}.$$

Let us also introduce the excursion sets A_u , which are simply those subsets of the sphere where the field is above some given value u :

$$A_u(f) := \{ x \in \mathbb{S}^2 : f(x) \geq u \}.$$

The idea is to compute the Lipschitz-Killing Curvatures on the (random) excursion sets, and then compare their observed values on real data with their expectation under Gaussianity and isotropy. It could be imagined that computing the latter might be a daunting task; on the contrary, it turns out that a completely explicit expression holds for random fields defined on general manifolds. In particular, the following Gaussian Kinematic Formula holds:

$$\mathbb{E} [\mathcal{L}_i(A_u(f))] = \sum_{k=0}^{2-i} \begin{bmatrix} k+i \\ k \end{bmatrix} \mathcal{L}_{k+i}(\mathbb{S}^2) \rho_k(u) \mu^{k/2},$$

where we have introduced the flag coefficients

$$\begin{bmatrix} d \\ k \end{bmatrix} = \binom{d}{k} \frac{\omega_d}{\omega_k \omega_{d-k}}$$

and the functions

$$\begin{aligned} \rho_0(u) &= 1 - \Phi(u), \\ \rho_k(u) &= \frac{1}{(2\pi)^{\frac{k+1}{2}}} H_{k-1}(u) \exp\left(-\frac{u^2}{2}\right), \text{ for } k \geq 1, \end{aligned}$$

where $\Phi(\cdot)$ denotes the standard Gaussian cumulative distribution whereas $H_k(u)$ stands for the Hermite polynomials, given by

$$H_k(u) = (-1)^k \exp\left(\frac{u^2}{2}\right) \frac{d^k}{du^k} \exp\left(-\frac{u^2}{2}\right) = (-1)^k \frac{1}{\phi(u)} \frac{d^k}{du^k} \phi(u) ;$$

here, $\phi(u)$ denotes as usual the standard Gaussian probability distribution. The first Hermite polynomials are $H_0(u) = 1$, $H_1(u) = u$, $H_2(u) = u^2 - 1$.

In particular, we obtain the following values for the case of the excursion area, the boundary length and the Euler-Poincaré characteristic:

$$\begin{aligned} \mathbb{E}[\mathcal{L}_2(A_u(f))] &= 4\pi(1 - \Phi(u)) , \\ \mathbb{E}[\mathcal{L}_1(A_u(f))] &= \pi \exp\left(-\frac{u^2}{2}\right) \mu^{1/2} , \\ \mathbb{E}[\mathcal{L}_0(A_u(f))] &= 2[u\phi(u)\mu + 1 - \Phi(u)] \end{aligned}$$

It turns out to be especially convenient to compute Lipschitz-Killing Curvatures on the needlelet components of the random fields, \tilde{T}_j . Indeed, in these circumstances, the expected values are simply obtained by replacing the needlelet covariance derivative for the parameter μ , which is simply given by:

$$\mu_j^2 := \sum_{\ell} \frac{2\ell + 1}{4\pi} \frac{\lambda_{\ell}}{2} b^2 \left(\frac{\ell}{B^j}\right) C_{\ell} .$$

The main advantage is that it can be shown that the variances of Lipschitz-Killing Curvatures decay to zero and a Central Limit Theorem holds in the high frequency limit, see, *e.g.*, Cammarota & Marinucci (2015), Shevchenko & Todino (2023) and the references therein. We have that

$$\frac{\mathcal{L}_i(A_u(\tilde{T}_j)) - \mathbb{E}[\mathcal{L}_i(A_u(\tilde{T}_j))]}{\sqrt{\text{Var}[\mathcal{L}_i(A_u(\tilde{T}_j))]} } \rightarrow_d N(0, 1) , \text{ as } B^j \rightarrow \infty , i = 0, 1, 2 .$$

Moreover, we have

$$\text{Var} \left[\frac{\mathcal{L}_i(A_u(\tilde{T}_j))}{\mathbb{E}[\mathcal{L}_i(A_u(\tilde{T}_j))]} \right] = O\left(\frac{1}{B^{2j}}\right) , \text{ as } j \rightarrow \infty .$$

These results prove that, in the high-frequency limit, the Lipschitz-Killing Curvatures converge to their expected values even on a single realization of a Gaussian isotropic map, and the fluctuations follow Gaussian behaviour, thus allowing for standard chi-square testing procedures for goodness-of-fit. This is yet another form of high-frequency ergodicity, as discussed in the previous section for the empirical distribution of critical points.

The values of the three Minkowski Functionals can be seen in **Figure 4**, including the theoretical expectation and both the mean and standard deviation on 100 simulations. The three Minkowski Functionals are shown for a large scale needlelet component ($B = 2$, $j = 3$, $\ell_{mean} = 8$), as well as the evolution of the standard deviation with needlelet scale; the trend closely resembles $\ell^{-1} \sim \frac{1}{B^j}$, as expected.

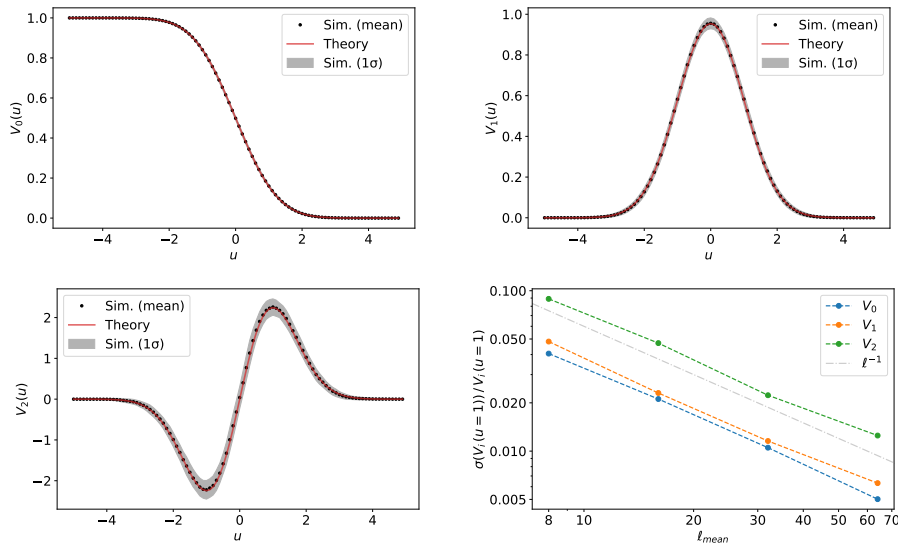


Figure 4

The results of the three Minkowski Functionals on needlet components of spherical fields. In all cases, the theory is compared with the mean and standard deviation of 100 Gaussian isotropic simulations. Top left, top right, and bottom left show the first, second, and third Minkowski Functionals as a function of threshold, for a low multipole needlet component ($B = 2$, $j = 3$, $\ell_{mean} = 8$). Bottom right shows the trend of the relative standard deviation of these statistics with respect to the size of the needlet considered, shown at $u = 1$ as an example; this is compared to the theoretically expected ℓ^{-1} trend.

These ideas have been applied in a series of papers, including an analysis on needlet components of Planck maps (Planck Collaboration 2020e). They find that the assumption of Gaussianity and isotropy of the foreground-cleaned maps is consistent with the empirical evidence: the Minkowski Functionals evaluated on the Planck CMB data are compatible with the results on realistic simulations at the 2σ level across different needlet frequencies (see also Planck Collaboration 2020f, for a study on Non-Gaussianity on Planck data).

Finally, it is worth noting that Minkowski Functionals, as well as other higher-order statistics, are being explored in several spherical fields within Cosmology. This is in order to extract more information from the possible non-Gaussianities of the fields, as this information is unavailable when using only the angular power spectrum. Some applications include Galactic foregrounds (Krachmalnicoff & Puglisi 2021, Martire et al 2023), maps of the gravitational lensing of the CMB due to general relativity (Euclid Collaboration 2023, Grewal et al 2022, Zürcher et al 2021), and the distribution of matter in the Universe, using either the galaxy distribution (Appleby et al 2022, Liu et al 2023) or observations of the emission of neutral H in the 21cm line (Spina et al 2021).

6. DIRECTIONS FOR FURTHER RESEARCH

The analysis of CMB temperature maps has now been very deeply explored in the last 20 years and, hence, a wide variety of tools and techniques are available for data analysis.

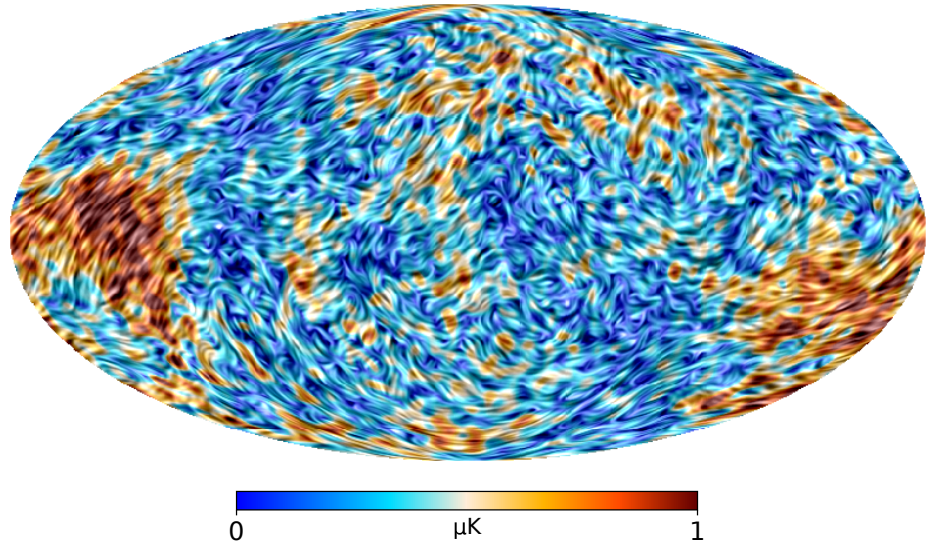


Figure 5

CMB polarization, as measured by the Planck satellite. Given that this is a spin 2 field on the sphere, we represent the modulus and direction: the polarization modulus is represented by the background colors, whereas the direction of the polarization is represented through unoriented lines, which constitute the texture of the image. Both modulus and direction have been smoothed with a Gaussian kernel at $fwhm = 4^\circ$ for visualization purposes.

The next couple of decades will present more sophisticated and mathematically challenging issues. Among these, a special mention must be devoted to CMB polarization data, which will be the object of several ground-based and satellite experiments, such as the Simons Observatory, ACT, or LiteBIRD, among others; see Hazumi et al (2020) and the references therein.

It is not easy to do justice to the mathematical complexity of polarization random fields at an introductory level. In a nutshell, the point is that the incoming photons making up CMB oscillate in the plane orthogonal to their travelling direction (as a standard consequence of Maxwell's equations of electromagnetism). Because of these oscillations, they can be understood as drawing unoriented lines on the tangent plane of every point in the celestial sphere. This line bundle can indeed be observed: see **Figure 5** for a visualization of CMB polarization (modulus and direction), and **Figure 6** for a visualization of the polarization direction over the temperature map; both figures with data measured by the Planck Satellite.

Mathematically, this can be modeled by considering polarization data as a realization of a random spin fiber bundle, as discussed for instance in Geller & Marinucci (2010), Leonenko & Sakhno (2012), Malyarenko (2013), Baldi & Rossi (2014), Stecconi (2022), Lerario et al (2022). The idea of spin fiber bundles was first introduced in a classical paper by Newman & Penrose (1966), where it is argued that a quantity $f_s(x)$ behaves as a spin bundle of order s if it transforms as follows under a rotation of γ radians of the tangent

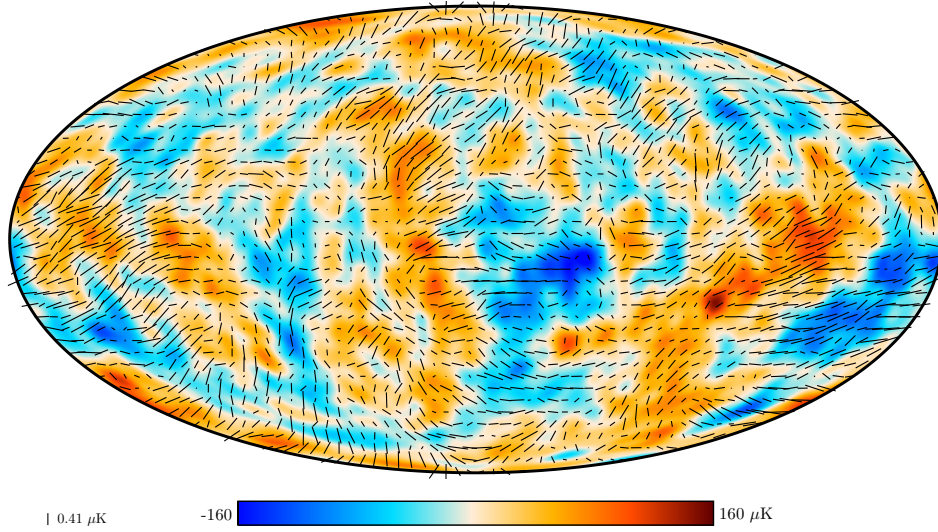


Figure 6

CMB temperature and direction of polarization, as measured by the Planck satellite. The color represents the value of the CMB temperature, while the unoriented lines represent the direction of the polarization. Both the temperature and the polarization direction have been smoothed with a Gaussian kernel at $fwhm = 5^\circ$ for visualization purposes. Figure reproduced from Planck Collaboration (2020a); copyright 2020 by The European Southern Observatory.

plane at x :

$$f'_s(x) = \exp(is\gamma) f_s(x) , \quad \gamma \in [0, 2\pi) .$$

In the case of line bundles, $s = 2$. Indeed, polarization at any point $x \in \mathbb{S}^2$ is invariant with respect to rotations of π radians (*i.e.*, 180 degrees). Spin random fields could also be seen as tensor-valued, see again Leonenko & Sakhno (2012), Malyarenko (2013) and the references therein. We note that it is also possible to give a spectral representation theorem (Geller & Marinucci 2010, Baldi & Rossi 2014) for spin random fields, which takes the form

$$f_s(x) = \sum_{\ell, m} a_{\ell m; 2} Y_{\ell m; 2}(x) , \quad (6)$$

where we have introduced the spin spherical harmonics and the spin raising operators

$$Y_{\ell m; 2}(x) = \partial_1 \partial_0 Y_{\ell m} ,$$

$$\partial_0 := \left(\frac{\partial}{\partial \theta} + \frac{i}{\sin \theta} \frac{\partial}{\partial \varphi} \right) , \quad \partial_1 := -\sin \theta \left(\frac{\partial}{\partial \theta} + \frac{i}{\sin \theta} \frac{\partial}{\partial \varphi} \right) \frac{1}{\sin \theta} .$$

The expansion in Equation 6 must again be taken with some care, as both the left and right-hand sides are not invariant to change of local coordinates in the tangent plane, even if the coordinates for $x \in \mathbb{S}^2$ remain the same.

The analysis of polarization data has an enormous importance for Cosmology. In short, polarization can provide a compelling proof of the existence of primordial gravitational waves, which would constitute an impressive verification of the key prediction of Inflation,

a theorized epoch of fast expansion in the very Early Universe (the first 10^{-32} seconds of the Universe). Other interesting aspects that can be studied with polarization involve the existence of a “reionization bump” in the angular power spectrum and the presence of weak gravitational lensing effects. However, polarization data are much fainter than the CMB temperature, and map-making and foreground removal are especially challenging, as proved, for instance, by the joint analysis of the Bicep/KECK and Planck team in Paoletti et al (2022).

To conclude this paper, we list a number of very challenging tasks, mostly related to the analysis of polarization data discussed in this section. These are likely to require major statistical efforts in the next ten years.

1. The implementation of techniques for map-making in polarization. This task is especially difficult because much less is known about the emission of astrophysical foreground sources in polarization with respect to temperature data; some attempts have been made to address these issues by means of neural network techniques (Krachmalnicoff & Puglisi 2021), but the field is still largely open for research. Very recently, attempts have been made to extend the ideas of NILC and its generalizations to the polarization framework, as in Carones et al. (2022b), Carones et al (2022c).
2. The development of goodness-of-fit tests for the assumptions of Gaussianity and isotropy is definitely a very urgent issue, as shown by the misclassification of Galactic dust emissions in some recent analysis of polarization data. The implementation on polarization data of Lipschitz-Killing Curvatures is made difficult by the fact that the definition of excursion sets is much more subtle in the case of fiber bundles: a possible approach is to focus on the squared norm of spin data, which is a scalar quantity following a chi-square distribution with two degrees of freedom. This is the approach followed by Carones et al (2022a), where the expected values of these functionals were also derived, exploiting results by Lerario et al (2022). Much remains to be done to investigate the statistical properties of such functionals in this framework: for instance, nothing is currently known about their asymptotic variance nor asymptotic distributions.
3. An alternative approach to polarization data can be pursued by lifting the field on the group of rotations $SO(3)$ where it is a scalar-valued (but anisotropic) field; see Stecconi (2022) for a mathematical discussion. In this case, the machinery by Adler & Taylor (2007) to compute the expected values of Lipschitz-Killing Curvatures becomes much more challenging, because the fields are no longer isotropic. However, to leading order, the main results are addressed in Carrón Duque et al (2023). Computation of variances and limiting distributions are still completely open for research.
4. A different approach for the derivation of statistics based on geometric and topological functionals (including Betti numbers) is pursued in Lerario et al (2022), where the excursion sets are given a much more general characterization in terms of the behaviour of the field, its gradient and Hessian, suitably defined for the spin case. Although this approach has made possible the calculation of some expected values, nothing is currently known on the variance and distribution of these statistics.
5. The sparsity of foreground components in the needlet domain could be exploited to improve its estimation and removal, as done by Oppizzi et al (2020) in CMB temperature. The relevant needlet and wavelet construction is known in polarization (Geller & Marinucci 2010) but the implementation of thresholding and other sparsity

enforcing techniques is still open for research and applications.

6. Very little is currently known about polarized point sources. The extension to spin data of the STEM procedure that we discuss in Section 4 for the scalar case therefore seems a very natural goal. However, a number of tools are still to be derived, starting from the distribution of local maxima for spin-valued random fields (in either of the approaches that we envisaged before, *i.e.*, either considering the corresponding norms as chi-square fields or searching for maxima in the anisotropic field on $SO(3)$).
7. With a more novel approach, considering that polarization observations are collected on many different frequency channels, it may be possible to address the foreground estimation issue in the framework of functional data analysis on the sphere. This area is completely open for research, even for the scalar (temperature) case: an attempt to consider statistical analysis for data on the sphere, which take values in a Hilbert space, has been very recently given by Caponera (2022).

This list of topics is by no means exhaustive, but we hope it will be enough to motivate some readers to get interested in this challenging and fascinating area of research.

DISCLOSURE STATEMENT

The authors are not aware of any affiliations, memberships, funding, or financial holdings that might be perceived as affecting the objectivity of this review.

ACKNOWLEDGMENTS

The research by JC has been supported by the InDark INFN project. The research by DM has been supported by the MUR Department of Excellence Programme MatMotTov.

LITERATURE CITED

- Adler RJ, Taylor JE. 2007. *Random Fields and Geometry*, Springer.
- Adler RJ, Taylor JE. 2011. *Topological complexity of smooth random functions*. Lecture Notes in Mathematics, 2019
- Atkinson K, Han W. 2012. *Spherical harmonics and approximations on the unit sphere: an introduction*. Lecture Notes in Mathematics, 2044. Springer.
- Appleby S, Park C, Pranav P, Hong SE, Hwang HS, Kim J, Buchert T. 2022. Minkowski Functionals of SDSS-III BOSS: Hints of Possible Anisotropy in the Density Field? *The Astrophysical Journal*, 928(2):108.
- Axelsson M, Ihle HT, Scodeller S, Hansen FK. 2015. Testing for foreground residuals in the Planck foreground cleaned maps: A new method for designing confidence masks, *Astronomy and Astrophysics*, 578:A44.
- Baldi P, Kerkycharian G, Marinucci D, Picard D. 2009a. Asymptotics for Spherical Needlets, *Annals of Statistics*, 37:1150-71.
- Baldi P, Kerkycharian G, Marinucci D, Picard D. 2009b. Subsampling needlet coefficients on the sphere, *Bernoulli*, 15:438-63.
- Baldi P, Marinucci D. 2007. Some characterizations of the spherical harmonics coefficients for isotropic random fields. *Statist. Probab. Lett.* 77(5):490-96.
- Baldi P, Rossi M. 2014. Representation of Gaussian isotropic spin random fields. *Stochastic Process. Appl.* 124(5):1910-41.
- Benjamini Y, Hochberg Y. 1995. Controlling the false discovery rate: a practical and powerful approach to multiple testing. *J. Roy. Statist. Soc. Ser. B*, 57:289-300.

- Paoletti D, Finelli F, Valiviita J, Hazumi M. 2022. Planck and BICEP/Keck Array 2018 constraints on primordial gravitational waves and perspectives for future B -mode polarization measurements, *Physical Review D*, 106(8),083528
- Bobin J, Sureau F, Starck JL, Rassat A, Paykari P. 2014. Joint Planck and WMAP CMB Map Reconstruction, *Astronomy and Astrophysics*, 563:A105.
- Brockwell PJ, Davis RA. 2006. *Time series: theory and methods*. Reprint of the second (1991) edition. Springer Series in Statistics. Springer, New York.
- Cammarota V, Marinucci D. 2015. The stochastic properties of ℓ^1 -regularized spherical Gaussian fields. *Appl. Comput. Harmon. Anal.* 38(2):262–83.
- Cammarota V, Marinucci D, Wigman I. 2016. On the distribution of the critical values of random spherical harmonics, *Journal of Geometric Analysis*, 26:3252–324.
- Caponera A. 2022. Asymptotics for isotropic Hilbert-valued spherical random fields. arXiv:2212.02329
- Carones A, Carrón Duque J, Marinucci D, Migliaccio M, Vittorio N. 2022a. Minkowski Functionals of CMB polarisation intensity with Pynkowski: theory and application to Planck data. arXiv:2211.07562.
- Carones A, Migliaccio M, Marinucci D, Vittorio N. 2022b. Analysis of NILC performance on B-modes data of sub-orbital experiments. arXiv:2208.12059.
- Carones A, Migliaccio M, Puglisi G, Baccigalupi C, Marinucci D, Vittorio N, Poletti D. 2022c. Multi-Clustering Needlet-ILC for CMB B-modes component separation. arXiv:2212.04456.
- Carrón Duque J, Buzzelli A, Fantaye Y, Marinucci D, Schwartzman A, Vittorio N. 2019. Point Source Detection and False Discovery Rate Control on CMB Maps, *Astronomy and Computing*, 28:100310
- Carrón Duque J, Carones A, Marinucci D, Migliaccio M, Vittorio N. 2023. Minkowski Functionals in $SO(3)$ for spin-2 CMB polarisation fields. arXiv:2301.13191.
- Cheng D, Cammarota V, Fantaye Y, Marinucci D, Schwartzman A. 2020. Multiple testing of local maxima for detection of peaks on the (celestial) sphere. *Bernoulli* 26(1):31–60.
- Cheng D, Schwartzman A. 2015. Distribution of the height of local maxima of Gaussian random fields. *Extremes*, 18:213–40.
- Cheng D, Schwartzman A. 2017. Multiple testing of local maxima for detection of peaks in random fields. *Ann. Statist.* 45(2):529–56.
- Cheng D, Schwartzman A. 2018. Expected number and height distribution of critical points of smooth isotropic Gaussian random fields. *Bernoulli* 24(4B):3422–46.
- Dodelson S. 2003. *Modern Cosmology*, Academic Press.
- Durrer R. 2008. *The Cosmic Microwave Background*, Cambridge University Press.
- Euclid Collaboration. 2023. Euclid Preparation XXIX: Forecasts for 10 different higher-order weak lensing statistics. arXiv:2301.12890.
- Geller D, Mayeli A. 2009a. Continuous Wavelets on Compact Manifolds, *Math. Z.*, 262:895–927.
- Geller D, Mayeli A. 2009b. Nearly Tight Frames and Space-Frequency Analysis on Compact Manifolds, *Math. Z.*, 263:235–64.
- Geller D, Mayeli A. 2009c. Besov Spaces and Frames on Compact Manifolds, *Indiana Univ. Math. J.*, 58:2003–42.
- Geller D, Marinucci D. 2010. Spin wavelets on the sphere. *J. Fourier Anal. Appl.* 16(6):840–84.
- Górski KM, Hivon E, Banday AJ, Wandelt BD, Hansen FK, Reinecke M, Bartelmann M. 2005. HEALPix: A Framework for High-Resolution Discretization and Fast Analysis of Data Distributed on the Sphere, *Astrophysical Journal*, 699:759–71.
- Grewal N, Zuntz J, Tröster T, Amon A. 2022. Minkowski Functionals in Joint Galaxy Clustering & Weak Lensing Analyses, *The Open Journal of Astrophysics*, 5.
- Hazumi M, Ade PAR, Adler A, Allys E, Arnold K, et al. 2022. LiteBIRD satellite: JAXA's new strategic L-class mission for all-sky surveys of cosmic microwave background polarization. *Proceedings of the SPIE*, 11443:114432F.

- Krachmalnicoff N, Puglisi G. 2021. ForSE: a GAN based algorithm for extending CMB foreground models to sub-degree angular scales, *The Astrophysical Journal*. 911:42.
- Liu W, Jiang A, Fang W. 2023. Probing massive neutrinos with the Minkowski functionals of the galaxy distribution, arXiv:2302.08162.
- Leonenko N, Sakhno L. 2012. On spectral representations of tensor random fields on the sphere. *Stoch. Anal. Appl.* 30(1):44–66.
- Lerario A, Marinucci D, Rossi M, Stecconi M. 2022. Geometry and topology of spin random fields. arXiv:2207.08413
- Loh WL. 2005. Fixed-Domain Asymptotics for a Subclass of Matérn-type Gaussian Random Fields, *Annals of Statistics*, 33:2344–94.
- Loh WL. 2015. Estimating the smoothness of a Gaussian random field from irregularly spaced data via higher-order quadratic variations, *Annals of Statistics*, 43:2766–94.
- Malyarenko A. 2013. *Invariant random fields on spaces with a group action*. Probability and its Applications (New York). Springer, Heidelberg
- Marinucci D, Peccati G. 2011. *Random Fields on the Sphere. Representation, Limit Theorem and Cosmological Applications*, Cambridge University Press
- Marinucci D, Peccati G. 2013. Mean Square Continuity on Homogeneous Spaces of Compact Groups, *Electronic Communications in Probability*. 18(37):1–10.
- Marinucci D, Pietrobon D, Balbi A, Baldi P, Cabella P, et al. 2008. Spherical Needlets for CMB Data Analysis, *Monthly Notices of the Royal Astronomical Society*, 383:539–45.
- Martire FA, Banday AJ, Martínez-González E, Barreiro RB. 2023. Morphological Analysis of the Polarized Synchrotron Emission with WMAP and Planck. arXiv:2301.08041.
- Narcowich FJ, Petrushev P, Ward JD. 2006a. Localized Tight Frames on Spheres, *SIAM Journal of Mathematical Analysis* , 38:574–94.
- Narcowich FJ, Petrushev P, Ward JD. 2006b. Decomposition of Besov and Triebel-Lizorkin Spaces on the Sphere, *Journal of Functional Analysis*, 238:530–64.
- Newman ET, Penrose R. 1966. Note on the Bondi-Metzner-Sachs group. *J. Mathematical Phys.* 7:863–70.
- Oppizzi F, Renzi A, Liguori M, Hansen FK, Baccigalupi C, et al. 2020. Needlet Thresholding Methods in Component Separation, *Journal of Cosmology and Astroparticle Physics*. 3:054.
- Planck Collaboration. 2015. Planck 2015. XXVI. The second Planck catalogue of compact sources, *Astronomy and Astrophysics*. 594:A26.
- Planck Collaboration. 2020a. Planck 2018 results I. Overview, and the cosmological legacy of Planck, *Astronomy and Astrophysics*. 641:A1.
- Planck Collaboration. 2020b. Planck 2018 results IV. Diffuse component separation, *Astronomy and Astrophysics*. 641:A4.
- Planck Collaboration. 2020c. Planck 2018 results V. CMB power spectra and likelihoods, *Astronomy and Astrophysics*. 641:A5.
- Planck Collaboration. 2020d. Planck 2018 results VI. Cosmological parameters, *Astronomy and Astrophysics*. 641:A6.
- Planck Collaboration. 2020e. Planck 2018 results VII. Isotropy and Statistics of the CMB, *Astronomy and Astrophysics*. 641:A7.
- Planck Collaboration. 2020f. Planck 2018 results IX. Constraints on primordial non-Gaussianity, *Astronomy and Astrophysics*. 641:A9.
- Remazeilles M, Delabrouille J, Cardoso JF. 2011. Foreground component separation with generalized Internal Linear Combination, *Monthly Notices of the Royal Astronomical Society*, 418(1):467–76.
- Scodeller S, Rudjord O, Hansen FK, Marinucci D, Geller D, Mayeli A. 2011. Introducing Mexican needlets for CMB analysis: Issues for practical applications and comparison with standard needlets, *Astrophysical Journal*. 733:121.
- Scodeller S, Hansen FK, Marinucci D. 2012. Detection of new point sources in WMAP 7 year data

- using internal templates and needlets, *Astrophysical Journal*, 753:27.
- Scodeller S, Hansen FK. 2012. Masking versus removing point sources in CMB data: the source corrected WMAP power spectrum from new extended catalogue, *Astrophysical Journal*, 761:119.
- Schwartzman A, Gavrilov Y, Adler RJ. 2011. Multiple testing of local maxima for detection of peaks in 1D, *Annals of Statistics*, 39:3290–319.
- Shevchenko R, Todino AP. 2023. Asymptotic behaviour of level sets of needlet random fields. *Stochastic Process. Appl.* 155:268–318.
- Spina B, Porciani C, Schimd C. 2021. The HI-halo mass relation at redshift $z \sim 1$ from the Minkowski functionals of 21-cm intensity maps. *Monthly Notices of the Royal Astronomical Society*, 505(3):3492-504
- Stecconi M. 2022. Isotropic random spin weighted functions on \mathbb{S}^2 vs isotropic random fields on \mathbb{S}^3 . *Theory Probab. Math. Statist.* 107:77–109.
- Vittorio, N. (2018) *Cosmology*, CRC Press.
- Zurcher D, Fluri J, Sgier R, Kacprzak T, Refregier A. 2021. Cosmological forecasts for non-Gaussian statistics in Large-Scale Weak Lensing Surveys. *Journal of Cosmology and Astroparticle Physics*, 2021(01):028

A. SPHERICAL HARMONICS AND THEIR MAIN PROPERTIES

In this Appendix, we discuss briefly the formalism of Fourier analysis on the sphere, and we introduce the main properties of spherical harmonics. Let us consider first the change of variables into spherical coordinates $(x, y, z) = (r \sin \theta \cos \varphi, r \sin \theta \sin \varphi, r \cos \theta)$, where $r^2 = x^2 + y^2 + z^2$, $\theta \in [0, \pi]$, $\varphi \in [0, 2\pi)$. With this change of coordinates, the 3-dimensional Laplacian operator $\Delta_{\mathbb{R}^3} = \frac{\partial^2}{\partial x^2} + \frac{\partial^2}{\partial y^2} + \frac{\partial^2}{\partial z^2}$ takes the form

$$\frac{1}{r^2} \frac{\partial}{\partial r} r^2 \frac{\partial}{\partial r} + \frac{1}{r^2} \Delta_{\mathbb{S}^2}, \text{ where } \Delta_{\mathbb{S}^2} = \frac{1}{\sin \theta} \frac{\partial}{\partial \theta} \sin \theta \frac{\partial}{\partial \theta} + \frac{1}{\sin^2 \theta} \frac{\partial^2}{\partial \varphi^2};$$

the operator $\Delta_{\mathbb{S}^2}$ is called the spherical Laplacian. The idea is to decompose the space of square integrable functions on the sphere, $L^2(\mathbb{S}^2)$, into an orthonormal system of polynomials, restricted to live on the unit sphere. We first consider homogeneous polynomials of order ℓ , *i.e.*, linear combinations of terms of the form $p_\ell(x, y, z) = x^{\alpha_1} y^{\alpha_2} z^{\alpha_3}$, with $\alpha_1 + \alpha_2 + \alpha_3 = \ell$. It is possible to show that the space of homogeneous polynomials of degree ℓ can be decomposed as

$$Q_\ell(x, y, z) = H_\ell(x, y, z) + r^2 H_{\ell-2}(x, y, z) + r^4 H_{\ell-4}(x, y, z) + \dots$$

where $H_\star(x, y, z)$ denotes the space of harmonic polynomials, *i.e.*, such that $\Delta_{\mathbb{R}^3} h(x, y, z) \equiv 0$ for all $h \in H_\star$. Because we are interested in the restrictions to the sphere, it is hence clearly enough to focus on polynomials that are both homogeneous and harmonic. Now note that any homogeneous polynomial can be written in spherical coordinates as $p_\ell(r, \theta, \varphi) = r^\ell Y_\ell(\theta, \varphi)$, leading to

$$\begin{aligned} & \left\{ \frac{1}{r^2} \frac{\partial}{\partial r} r^2 \frac{\partial}{\partial r} + \frac{1}{r^2} \Delta_{\mathbb{S}^2} \right\} p_\ell(r, \theta, \varphi) \\ &= r^{\ell-2} \ell(\ell+1) Y_\ell(\theta, \varphi) + r^{\ell-2} \Delta_{\mathbb{S}^2} Y_\ell(\theta, \varphi) = 0. \end{aligned}$$

In other words, we must search for eigenfunctions of the spherical Laplacian with eigenvalue $\lambda_\ell = -\ell(\ell+1)$.

The following properties of spherical harmonics are important for a proper understanding of the statistical issues and techniques reviewed in this paper.

1. The space of eigenfunctions corresponding to the ℓ -th eigenvalue ($\lambda_\ell = -\ell(\ell + 1)$) has dimensions $2\ell + 1$. Eigenfunctions belonging to different eigenspaces are orthogonal; indeed, recalling that the Laplacian is a self-adjoint operator (*i.e.*, $\int_{\mathbb{S}^2} (\Delta_{\mathbb{S}^2} f)(x)g(x)dx = \int_{\mathbb{S}^2} f(x)(\Delta_{\mathbb{S}^2} g)(x)dx$, for all $f, g \in L^2(\mathbb{S}^2)$) we easily have that

$$\begin{aligned} \langle Y_\ell, Y_{\ell'} \rangle_{L^2(\mathbb{S}^2)} &= \int_{\mathbb{S}^2} Y_\ell(x) \overline{Y_{\ell'}(x)} dx = -\frac{1}{\ell(\ell+1)} \int_{\mathbb{S}^2} (\Delta_{\mathbb{S}^2} Y_\ell)(x) \overline{Y_{\ell'}(x)} dx \\ &= -\frac{1}{\ell(\ell+1)} \int_{\mathbb{S}^2} Y_\ell(x) (\Delta_{\mathbb{S}^2} \overline{Y_{\ell'}})(x) dx \\ &= \frac{\ell'(\ell'+1)}{\ell(\ell+1)} \int_{\mathbb{S}^2} Y_\ell(x) \overline{Y_{\ell'}(x)} dx = \frac{\ell'(\ell'+1)}{\ell(\ell+1)} \langle Y_\ell, Y_{\ell'} \rangle_{L^2(\mathbb{S}^2)}, \end{aligned}$$

which implies the result.

2. A standard orthonormal basis for these spaces is formed by the so-called (complex-valued) Fully Normalized Spherical Harmonics, defined by

$$\begin{aligned} Y_{\ell m}(\theta, \varphi) &= \sqrt{\frac{2\ell+1}{4\pi}} \sqrt{\frac{(\ell-m)!}{(\ell+m)!}} P_{\ell m}(\cos \theta) \exp(im\varphi), \text{ for } m \geq 0, \\ Y_{\ell m}(\theta, \varphi) &= (-1)^m \overline{Y_{\ell, -m}}(\theta, \varphi) \text{ for } m < 0, \end{aligned}$$

where $m = -\ell, \dots, \ell$ and we have introduced the associated Legendre functions

$$P_{\ell m}(t) := \frac{1}{2^\ell \ell!} (1-t^2)^{m/2} \frac{d^{\ell+m}}{dt^{\ell+m}} (t^2-1)^\ell,$$

see Atkinson & Han (2012) and Marinucci & Peccati (2011) for more discussion and details.

3. In the special case where $m = 0$, the associated Legendre polynomials coincide with Legendre polynomials, defined by

$$P_\ell(t) := \frac{1}{2^\ell \ell!} \frac{d^\ell}{dt^\ell} (t^2-1)^\ell.$$

Legendre polynomials form an orthogonal base for the space of square integrable functions from $[-1, 1]$ into \mathbb{R} .

4. By construction, we have that

$$\int_{\mathbb{S}^2} Y_{\ell m}(x) \overline{Y_{\ell' m'}(x)} dx = \int_{\mathbb{S}^2} Y_{\ell m}(\theta, \varphi) \overline{Y_{\ell' m'}(\theta, \varphi)} \sin \theta d\varphi d\theta = \delta_\ell^{\ell'} \delta_m^{m'}. \quad (7)$$

The crucial properties of spherical harmonics are given by the so-called Addition Formula and Duplication Formula. The first holds for any system of orthogonal elements and states the following: given $x_1, x_2 \in \mathbb{S}^2$, we have that

$$\sum_{m=-\ell}^{\ell} Y_{\ell m}(x_1) \overline{Y_{\ell m}(x_2)} = \frac{2\ell+1}{4\pi} P_\ell(\langle x_1, x_2 \rangle), \quad (8)$$

see Atkinson & Han (2012), Theorem 2.9, or Marinucci & Peccati (2011), Section 3.4.2, for a proof. The duplication formula, on the other hand, can be stated as follows: for any $x_1, x_2 \in \mathbb{S}^2$, we have that

$$\int_{\mathbb{S}^2} \frac{2\ell+1}{4\pi} P_\ell(\langle x_1, x \rangle) \frac{2\ell+1}{4\pi} P_\ell(\langle x, x_2 \rangle) dx = \frac{2\ell+1}{4\pi} P_\ell(\langle x_1, x_2 \rangle). \quad (9)$$

The proof follows immediately by using eq 8 twice and eq 7.

The overwhelming majority of statistical results does not require any explicit manipulation of the analytic expressions for the $Y_{\ell m}(\cdot)$; these expressions are numerically implemented on packages such as HealPix (Górski et al 2005). On the other hand, Equations 7, 8, and 9 are the basis for nearly every theoretical argument in the analysis of spherical random fields.

B. THE SPECTRAL REPRESENTATION THEOREM

The Spectral Representation Theorem plays such a crucial role in the analysis of isotropic spherical random fields that we feel it is useful to give a proper statement and a sketch of its proof here. Let us first recall that a function $\Gamma(\cdot, \cdot) : \mathbb{S}^2 \times \mathbb{S}^2 \rightarrow \mathbb{R}$ is said to be non-negative if and only if for all $p \in \mathbb{N}$, $x_1, \dots, x_p \in \mathbb{S}^2$, and $\alpha_1, \dots, \alpha_p \in \mathbb{R}$ we have that

$$\sum_{j,k=1}^p \alpha_j \alpha_k \Gamma(x_j, x_k) \geq 0 .$$

Given that we are concerned with isotropic fields, we have that $\Gamma(x_j, x_k) = \Gamma(x'_j, x'_k)$ whenever $\langle x_j, x_k \rangle = \langle x'_j, x'_k \rangle$; in these cases we say that the function $\Gamma(\cdot, \cdot)$ is isotropic and, with some abuse of notation, we write $\Gamma(x_j, x_k) = \Gamma(\langle x_j, x_k \rangle)$. The next ingredient that we have to consider is Schoenberg's Theorem, which reads as follows:

Theorem 1 (Schoenberg). *Let $\Gamma(\langle x_1, x_2 \rangle) : \mathbb{S}^2 \times \mathbb{S}^2 \rightarrow \mathbb{R}$ be an isotropic, continuous, non-negative definite function. Then there exist a sequence of non-negative weights $\{C_\ell\}_{\ell=0,1,\dots}$ such that $\sum_{\ell=0}^{\infty} \frac{2\ell+1}{4\pi} C_\ell = \Gamma(\langle x, x \rangle) < \infty$ and*

$$\Gamma(\langle x_1, x_2 \rangle) = \sum_{\ell=0}^{\infty} \frac{2\ell+1}{4\pi} C_\ell P_\ell(\langle x_1, x_2 \rangle) ,$$

uniformly for all $x_1, x_2 \in \mathbb{S}^2$.

Therefore, the family of non-negative isotropic functions on $\mathbb{S}^2 \times \mathbb{S}^2$ can be identified with the covariance functions of isotropic random fields. Schoenberg's Theorem is hence a generalization of classical results by Herglotz and Bochner: it states that the autocovariance functions can be expressed as an inverse Fourier transform of the *angular power spectrum* $\{C_\ell\}_{\ell=0,1,\dots}$. The result requires the autocovariance function to be uniformly continuous; however, it was proved by Marinucci & Peccati (2013) that this is necessarily the case if the isotropic spherical random field is measurable.

Having in mind this result, the Spectral Representation Theorem can be stated as follows:

Theorem 2 (Spectral Representation). *Let $T : \Omega \times \mathbb{S}^2 \rightarrow \mathbb{R}$ be an isotropic random field on the sphere with finite variance. Then there exists a family of orthogonal random coefficients $\{a_{\ell m}\}_{m=-\ell,\dots,\ell; \ell=0,1,2,\dots}$ such that $\mathbb{E}[a_{\ell m} \overline{a_{\ell' m'}}] = \delta_\ell^{\ell'} \delta_m^{m'} C_\ell$ and*

$$T(x, \omega) = \sum_{\ell=0}^{\infty} \sum_{m=-\ell}^{\ell} a_{\ell m}(\omega) Y_{\ell m}(x) ,$$

where the equality holds both in the $L^2(\Omega)$ sense for fixed $x \in \mathbb{S}^2$ and in $L^2(\Omega \times \mathbb{S}^2)$.

Proof. (Sketch) A sketch of the proof can be given as follows. Denote by $\mathcal{H} = \overline{\text{span}} \{T(x), x \in \mathbb{S}^2\} \subset L^2(\Omega)$ the closure of the space generated by the linear combinations of $T(x)$, and define the linear isometry

$$D : \mathcal{H} \rightarrow L^2(\mathbb{S}^2), \quad D(T(x)) := \sum_{\ell=0}^{\infty} \frac{2\ell+1}{4\pi} \sqrt{C_\ell} P_\ell(\langle \cdot, x \rangle).$$

Finally, let us call $\mathcal{K} = \overline{\text{span}} \left\{ \sum_{\ell=0}^{\infty} \frac{2\ell+1}{4\pi} C_\ell P_\ell(\langle \cdot, x \rangle), x \in \mathbb{S}^2 \right\} \subset L^2(\mathbb{S}^2)$. It is readily seen that this application is indeed an isometry, in fact by Schoenberg's Theorem we have that

$$\begin{aligned} \mathbb{E}[T(x_1)T(x_2)] &= \langle T(x_1), T(x_2) \rangle_{L^2(\Omega)} = \sum_{\ell=0}^{\infty} \frac{2\ell+1}{4\pi} C_\ell P_\ell(\langle x_1, x_2 \rangle) \\ &= \int_{\mathbb{S}^2} \sum_{\ell=0}^{\infty} \frac{2\ell+1}{4\pi} \sqrt{C_\ell} P_\ell(\langle x_1, x \rangle) \sum_{\ell'=0}^{\infty} \frac{2\ell'+1}{4\pi} \sqrt{C_{\ell'}} P_{\ell'}(\langle x, x_2 \rangle) dx \\ &= \langle D(T(x_1)), D(T(x_2)) \rangle_{L^2(\mathbb{S}^2)}, \end{aligned}$$

using the duplication formula and the definition of the inner product in $L^2(\mathbb{S}^2)$. It is also readily seen, for instance by approximating the integral with Riemann sums, that we have

$$\begin{aligned} a_{\ell m}(\omega) &:= \int_{\mathbb{S}^2} T(x, \omega) \overline{Y_{\ell m}(x)} dx \in \mathcal{H}, \\ D(a_{\ell m}(\omega)) &= \int_{\mathbb{S}^2} D(T(x, \omega)) \overline{Y_{\ell m}(x)} dx = \int_{\mathbb{S}^2} \sum_{\ell=0}^{\infty} \frac{2\ell+1}{4\pi} C_\ell P_\ell(\langle \cdot, x \rangle) \overline{Y_{\ell m}(x)} dx = \sqrt{C_\ell} \overline{Y_{\ell m}(\cdot)}, \end{aligned}$$

using again 8 and 7; note that

$$\mathbb{E}[a_{\ell m} \overline{a_{\ell' m'}}] = \langle a_{\ell m}, a_{\ell' m'} \rangle_{L^2(\Omega)} = \left\langle \sqrt{C_\ell} \overline{Y_{\ell m}(\cdot)}, \sqrt{C_{\ell'}} \overline{Y_{\ell' m'}(\cdot)} \right\rangle_{L^2(\Omega)} = \delta_\ell^{\ell'} \delta_m^{m'} C_\ell.$$

Moreover, the application D is an isometry and thus injective and invertible, so that

$$\begin{aligned} T(x, \omega) &= D^{-1} \left(\sum_{\ell=0}^{\infty} \frac{2\ell+1}{4\pi} \sqrt{C_\ell} P_\ell(\langle \cdot, x \rangle) \right) \\ &= \sum_{\ell=0}^{\infty} \frac{2\ell+1}{4\pi} D^{-1} \left(\sqrt{C_\ell} \overline{Y_{\ell m}(\cdot)} \right) Y_{\ell m}(x) \\ &= \sum_{\ell=0}^{\infty} \sum_{m=-\ell}^{\ell} a_{\ell m}(\omega) Y_{\ell m}(x), \end{aligned}$$

where we have used, once again, linearity and Equation 8; the proof is then completed. \square

As a final remark, it follows from the proof that the spherical harmonic coefficients are always uncorrelated, and hence independent, in the Gaussian case. Surprisingly, the reverse turns out to be the case as well: for isotropic random fields, if the spherical harmonic coefficients are independent, then they are necessarily Gaussian, see Baldi & Marinucci (2007). Some ongoing research is devoted to provide further characterizations of the spherical harmonics coefficients.